BOREHOLE WAVE PROPAGATION IN ISOTROPIC AND ANISOTROPIC MEDIA III: ANISOTROPIC FORMATION

by

Ningya Cheng, C.H. Cheng, and M.N. Toksöz

Earth Resources Laboratory
Department of Earth, Atmospheric, and Planetary Sciences
Massachusetts Institute of Technology
Cambridge, MA 02139

ABSTRACT

In this paper we extend the 3-D finite difference method to simulate wave propagations in an anisotropic medium. The scheme is tested in the homogeneous medium. The finite difference results agree excellently with the analytic solutions of a point force source in the transversely isotropic medium. The finite difference synthetics are compared with ultrasonic lab measurements in a scaled borehole drilled along the X axis in an orthorhombic phenolite solid. Both monopole and dipole logs agree well.

The 3-D time domain finite difference method is applied to the fluid-filled borehole wave propagation problems in the anisotropic formation. The following results are obtained:

1. In a borehole drilled along the Z axis in a phenolite formation, the monopole log shows the P wave travelling with velocity v_{zz}. There are no shear-pseudo-Rayleigh wave arrivals. The dipole log is dominated by the single slow flexural mode.

2. In a borehole drilled along the Y axis in a phenolite formation, the monopole log shows the P wave travelling with velocity v_{yy}. There are shear-pseudo-Rayleigh wave arrivals shown on the monopole seismograms between the P and Stoneley waves due to the shear wave anisotropy. The anisotropy also causes the shear wave splitting in the dipole log. The two shear wave arrivals correspond to the fast and the slow flexural modes.

3. The disagreement between the shear wave velocity from the Stoneley wave inversion and the direct shear wave log velocity from field data is beyond the errors in the measurements. It is shown that the formation permeability is not the cause of the discrepancy. From the estimated "shear/pseudo-Rayleigh" phase velocities in the array full waveform log and the 3-D finite difference synthetics in the anisotropic formation, the discrepancy can be explained as shear wave anisotropy.

INTRODUCTION

The crust of the Earth is slightly anisotropic, which is related to geological processes. For example, anisotropy can be caused by aligned fractures in the rock. Knowledge of this anisotropy might help to determine stress or fluid flow directions. Fine layered sedimentary rocks possess transverse isotropy. Acoustic logging provides a technique to measure the anisotropy in the crust.

The effects of the formation anisotropy on the fluid-filled borehole wave propagation are studied by a number of authors. In the case of a transversely isotropic formation with the symmetry axis aligned with the borehole axis, White and Tongtaow (1981) studied the monopole and the dipole logs. Chan and Tsang (1983) examined the refracted waves in a radially layered transversely isotropic formation. Schmitt (1989) investigated the body waves and normal modes in a radially layered transversely isotropic and permeable formation. Leveille and Seriff (1989) and Nicoletis et al. (1990) determined the particle motion and the phase velocity of the Stoneley wave at the zero frequency limit in the case of transverse isotropy with a symmetry axis perpendicular to the borehole axis. Ellefsen (1990) developed the perturbation and finite element method to study borehole normal modes in a general anisotropic formation. Sinha et al. (1991) extended the perturbation method to compute borehole flexural waveforms in an anisotropic formation. Norris and Sinha (1993) also applied the perturbation method to derive Stoneley wave phase velocity in a weak anisotropy formation. Renlie and Raaen (1993) examined an acoustic log in a borehole surrounded by a formation with stress-relief-induced anisotropy, which is called radial transverse isotropy. Leslie and Randall (1992) extended their 2.5-D finite difference method to model acoustic wave propagation in a borehole penetrating a general anisotropic formation. The numerical examples are shown for a transversely isotropic formation. Ultrasonic experiments are performed on a scaled borehole model in a phenolite solid. The orthorhombic phenolite is approximated as a transversely isotropic solid. The lab measurements are compared with the 2.5-D finite difference dipole synthetics.

In this paper the 3-D time domain finite difference method is extended to include anisotropy. The finite difference results are compared with the analytic solutions in a transversely isotropic solid. Borehole wave propagations in the orthorhombic formation are simulated with a borehole drilled in different directions. Finite difference simulations are compared with the ultrasonic lab measurements using a scaled borehole model.

FINITE DIFFERENCE METHOD IN AN ANISOTROPIC MEDIUM

Wave propagation in an anisotropic elastic medium can also be described by the equation of motion:

$$\rho \frac{\partial^2}{\partial t^2} u_i = \tau_{ij,j} \tag{1}$$

where ρ is the density, u_i is the displacement vector, and τ_{ij} is the stress tensor. The generalized Hooke's law links the stress tensor τ_{ij} to the strain tensor ε_{ij} in a linear fashion:

$$\tau_{ij} = c_{ijkl}\varepsilon_{kl} \tag{2}$$

where c_{ijkl} is the fourth-order elastic constant tensor. The strain tensor is defined as:

$$\varepsilon_{ij} = \frac{1}{2}(u_{i,j} + u_{j,i}). \tag{3}$$

In order to simplify the elastic constants tensor in Cartesian coordinates the strain tensor is replaced by the strain vector defined as

$$E = \begin{pmatrix} \varepsilon_{xx} \\ \varepsilon_{yy} \\ \varepsilon_{zz} \\ 2\varepsilon_{yz} \\ 2\varepsilon_{xz} \\ 2\varepsilon_{xy} \end{pmatrix}. \tag{4}$$

The stress tensor is replaced by the stress vector

$$T = \begin{pmatrix} \tau_{xx} \\ \tau_{yy} \\ \tau_{zz} \\ \tau_{yz} \\ \tau_{xz} \\ \tau_{xy} \end{pmatrix}. \tag{5}$$

The fourth order elastic constant tensor can be replaced by a 6×6 symmetric stiffness matrix because of the symmetry property of the tensor:

$$C = \begin{pmatrix} c_{11} & c_{12} & c_{13} & c_{14} & c_{15} & c_{16} \\ & c_{22} & c_{23} & c_{24} & c_{25} & c_{26} \\ & & c_{33} & c_{34} & c_{35} & c_{36} \\ & & & c_{44} & c_{45} & c_{46} \\ & & & & c_{55} & c_{56} \\ \textit{symmetric} & & & & & c_{66} \end{pmatrix}. \tag{6}$$

Here the abbreviated subscript notations are used to reduce the four subscripts of the tensor. The relations between the full subscripts and the abbreviated subscripts in Cartesian coordinates are:

Full subscript (ij) or (kl)	Abbreviated subscripts (I)
xx	1
yy	2
zz	3
yz or zy	4
xz or zx	5
xy or yx	6 .

The generalized Hooke's law can be written in the matrix form as:

$$T = CE\,. \tag{7}$$

In this chapter, orthorhombic anisotropy with nine elastic constants is considered. The reasons are the following: orthorhombic anisotropy gives the most general case without the normal stress and the shear strain coupling. It can be straightforward to implement on the staggered grid used in Chapter 2 (for the general anisotropy case, some average schemes are needed to make a centered finite difference operator on the staggered grid due to the offset of the normal and the shear stress). For practical geophysical applications, orthorhombic anisotropy provides very good models for most actual rocks.

An orthorhombic solid has three perpendicular planes of symmetry. The stiffness matrix is

$$\begin{pmatrix} c_{11} & c_{12} & c_{13} & 0 & 0 & 0 \\ & c_{22} & c_{23} & 0 & 0 & 0 \\ & & c_{33} & 0 & 0 & 0 \\ & & & c_{44} & 0 & 0 \\ & & & & c_{55} & 0 \\ \textit{symmetric} & & & & & c_{66} \end{pmatrix}. \tag{8}$$

For example, some type of granites possess this kind of anisotropy.

A widely used anisotropic type is the transverse isotropy, which can be reduced from the orthorhombic system. It has one axis of rotational symmetry. This solid is represented by 5 independent elastic constants. The stiffness matrix is

$$\begin{pmatrix} c_{11} & c_{12} & c_{13} & 0 & 0 & 0 \\ & c_{11} & c_{13} & 0 & 0 & 0 \\ & & c_{33} & 0 & 0 & 0 \\ & & & c_{44} & 0 & 0 \\ & & & & c_{44} & 0 \\ \textit{symmetric} & & & & & c_{66} \end{pmatrix} \tag{9}$$

where $c_{12} = c_{11} - 2c_{66}$. Transverse isotropy is used to model rocks with aligned fractures, sedimentary rocks or the layered earth in which the layer thickness is much smaller than the wavelength.

Orthorhombic anisotropy can be reduced to the other types. For example, when $c_{11} = c_{22}$, $c_{23} = c_{13}$ and $c_{44} = c_{55}$, the orthorhombic system reduces to a 6 constants

tetragonal system. When $c_{11} = c_{22} = c_{33}$, $c_{44} = c_{55} = c_{66}$ and $c_{12} = c_{13} = c_{23}$, the orthorhombic system reduces to a 3 independent elastic constants cubic system.

When the elastic constants are not dependent on the orientation, the solid is called isotropy. There are two independent parameters. The stiffness matrix is

$$\begin{pmatrix} c_{11} & c_{13} & c_{13} & 0 & 0 & 0 \\ & c_{11} & c_{13} & 0 & 0 & 0 \\ & & c_{11} & 0 & 0 & 0 \\ & & & c_{44} & 0 & 0 \\ & & & & c_{44} & 0 \\ symmetric & & & & & c_{44} \end{pmatrix} \tag{10}$$

where $c_{11} = c_{13} + 2c_{44}$. Using Lamé constants, $c_{13} = \lambda$, $c_{44} = \mu$ and $c_{11} = \lambda + 2\mu$. This is the case we discussed in the previous papers.

Equation (1) and (7) are reformulated by using velocity and stress for the orthorhombic anisotropic medium. The first order hyperbolic equations in Cartesian coordinates can be written in their components form as

$$\begin{aligned} \rho\frac{\partial v_x}{\partial t} &= \frac{\partial \tau_{xx}}{\partial x} + \frac{\partial \tau_{xy}}{\partial y} + \frac{\partial \tau_{xz}}{\partial z} \\ \rho\frac{\partial v_y}{\partial t} &= \frac{\partial \tau_{xy}}{\partial x} + \frac{\partial \tau_{yy}}{\partial y} + \frac{\partial \tau_{yz}}{\partial z} \\ \rho\frac{\partial v_z}{\partial t} &= \frac{\partial \tau_{xz}}{\partial x} + \frac{\partial \tau_{yz}}{\partial y} + \frac{\partial \tau_{zz}}{\partial z} \end{aligned} \tag{11}$$

and

$$\begin{aligned} \frac{\partial \tau_{xx}}{\partial t} &= c_{11}\frac{\partial v_x}{\partial x} + c_{12}\frac{\partial v_y}{\partial y} + c_{13}\frac{\partial v_z}{\partial z} \\ \frac{\partial \tau_{yy}}{\partial t} &= c_{12}\frac{\partial v_x}{\partial x} + c_{22}\frac{\partial v_y}{\partial y} + c_{23}\frac{\partial v_z}{\partial z} \\ \frac{\partial \tau_{zz}}{\partial t} &= c_{13}\frac{\partial v_x}{\partial x} + c_{23}\frac{\partial v_y}{\partial y} + c_{33}\frac{\partial v_z}{\partial z} \\ \frac{\partial \tau_{xy}}{\partial t} &= c_{44}(\frac{\partial v_x}{\partial y} + \frac{\partial v_y}{\partial x}) \\ \frac{\partial \tau_{xz}}{\partial t} &= c_{55}(\frac{\partial v_x}{\partial z} + \frac{\partial v_z}{\partial x}) \\ \frac{\partial \tau_{yz}}{\partial t} &= c_{66}(\frac{\partial v_y}{\partial z} + \frac{\partial v_z}{\partial y}) . \end{aligned} \tag{12}$$

The above equations are discretized on the staggered grid shown in paper I. Because we only consider the orthorhombic anisotropic medium, the normal stress and shear strain are not related by Hooke's law. The finite difference operators, defined paper I, are properly centered. The first order time derivative is approximated by the second order finite difference operator and the first order space derivatives are approximated

by the fourth order finite difference operators. These operators are described in paper I. The medium parameters $c_{11}, c_{12}, c_{13}, c_{22}, c_{23}, c_{33}, c_{44}, c_{55}, c_{66}$ and ρ are assigned at the grid point $(m+\frac{1}{2}, n+\frac{1}{2}, k)$. In order to update the velocities, the needed density values are obtained from the average of two nearby assigned densities. In order to update the shear stress, the needed shear moduli are determined by four nearby assigned shear moduli using the harmonic average. This automatically puts the shear modulus zero at the fluid-solid boundary.

To control the grid dispersion and the grid anisotropy we adopt the same rule of thumb used in the paper I. The stable condition used to determine the time step size is

$$\Delta t < \frac{\Delta}{\sqrt{3} v_p (|\eta_1| + |\eta_2|)} \tag{13}$$

where v_p is the fastest quasi-P wave velocity in the model.

In order to simulate the infinite medium on a computer with limited memory we have to eliminate the reflections from the artificial boundaries. Higdon's absorbing boundary condition operator is generalized for an anisotropic medium

$$B = \prod_{j=1}^{m} (c_j \frac{\partial}{\partial t} - \alpha \frac{\partial}{\partial x}) \tag{14}$$

because in the anisotropic medium, the wave propagates with the different velocity in the different directions. The velocity α in the absorbing boundary condition is properly chosen according to the direction of the boundary. For example, for the boundary at $x = x_0$ for the P wave absorbing term we choose $\alpha = \sqrt{\frac{c_{11}}{\rho}}$ and for the boundary at $y = y_0$ for the P wave absorbing term we choose $\alpha = \sqrt{\frac{c_{22}}{\rho}}$.

Finally, a 3-D finite difference scheme for an orthorhombic medium is implemented on the nCUBE parallel computer by using the Grid Decomposition Package. The constants of the orthorhombic medium are stored in a small data array instead of ten full 3-D arrays so as to reduce the memory requirements. At every grid point an index file is searched to determine which constants will be used in the calculations.

COMPARISON WITH THE ANALYTIC SOLUTION

In this section the finite difference method is tested in a homogeneous transversely isotropic medium. The same test is used by Carcione et al. (1992) to verify their 3-D spectral scheme for wave propagation in anisotropic media.

The medium chosen for the test is Mesaverde clay shale (Thomsen, 1986). It is a transversely isotropic solid. The properties of the clay shale are listed in Table 1. The slowness surfaces are plotted in Figure 1. The 3-D slowness surfaces have azimuthal symmetry. The plotted 2-D section (X-Z plane) contains the symmetry axis. There are three types of wave: quasi-P, quasi-S and pure shear. Quasi-P and quasi-S are coupled.

The parameters used for the finite difference calculations are the following: A 70 × 70 × 200 grid with grid size of 4 cm and time step size 0.002 ms. The source is a point vertical force. The source time function is a Kelly wavelet at center frequency 2.5 kHz. The source-receiver distance is 4 m along the Z axis. The second order Higdon's absorbing boundary condition is used. The analytical solution of a vertical force acting along the symmetry axis of a transversely isotropic solid is given in Appendix A.

Figure 2 compares the normalized finite difference and the analytical solutions from the vertical force. The total time is 4 ms. The vertical velocity v_z is shown in the plot. The agreement is excellent. The two solutions are plotted separately in order to show the two waveforms. Figure 3 shows the wavefield snapshot of the vertical velocity v_z at time 1.6 ms. The 3-D image is sliced at the XZ, YZ and XY plane. The wavefield is symmetric about the Z axis. The wavefronts are no longer spherical because of the anisotropy. The seismogram and the snapshot show the good performance of Higdon's absorbing boundary condition in the anisotropic medium with properly chosen velocities.

BOREHOLE WAVE PROPAGATION IN AN ORTHORHOMBIC MEDIUM

In this section the 3-D time domain finite difference method is applied to the fluid-filled borehole wave propagation in an orthorhombic formation. The anisotropic elastic constants used here are obtained from phenolite XX-324. The phenolite possesses a strong anisotropy and can be described as an orthorhombic solid (Cheadle et al., 1991). The elastic constants of phenolite are determined from the lab velocity measurements. The monopole and dipole logs are simulated in the borehole drilled along the X, Y and Z axis. The finite difference synthetics are compared with the ultrasonic measurements in the scaled borehole model.

Elastic Constants of Phenolite

A cubic sample of the phenolite is used to do the property measurements (Zhu et al., 1993). The P and S wave velocities are measured along the three principal axes by using the compressional and shear wave transducers (Figure 4). The three principal axes are assigned as X, Y and Z. The velocity values are labeled with two indexes. The first is the direction of the propagation and the second is the direction of the particle motion. The six independent velocities can be used to determine six elastic constants along the diagonal of the stiffness matrix. Another three velocity measurements are needed to determine the three off-diagonal constants. The measuring is done between the opposite edges of the phenolite cube (Z. Zhu, 1993, personal communication). The propagation directions are at a 45 degree angle between two principal axes and perpendicular to the third. The results are listed in Table 2. Using the body wave phase velocity formulas given in Appendix B for the orthorhombic solid, nine elastic constants can be determined (Cheadle et al., 1991). The values are listed in Table 3. The slowness surfaces of phenolite can be recalculated by using these nine elastic constants. The 3-D slowness surface is sliced at the X-Y plane, the X-Z plane and the Y-Z plane. It is

shown in Figure 5. The anisotropy is very clear in the plot. The shear wave velocity anisotropy is about 28% and the P wave velocity anisotropy is about 30%.

Borehole Wave Propagation: Monopole

The monopole source response in a fluid-filled borehole with the phenolite solid as formation is calculated. The borehole fluid is water. Its velocity is 1500 m/s and the density is 1 gcm^{-3}. The borehole diameter is 0.24 m. It is numerically drilled along the Y axis. A $70 \times 300 \times 70$ grid is used for the calculations. The grid size is 1 cm and the time step is 0.001 ms. The monopole Kelly source at center frequency 5 kHz is located at (35,40,35) on the grid. The ten pressure receivers are located along the borehole center. The first receiver is 0.7 m away from the source and receiver spacing is 0.2 m.

The seismograms are plotted in Figure 6. The first P wave arrival is traveling with velocity v_{yy}, which is 3620 m/s. The large amplitude low frequency Stoneley wave is travelling with phase velocity about 1220 m/s. If the formation is isotropic and the shear wave velocity is 1390 m/s, the Stoneley wave phase velocity is about 1100 m/s. If the formation is isotropic and the shear wave velocity is 1940 m/s, the Stoneley wave phase velocity is about 1300 m/s. So the Stoneley wave velocity in the orthorhombic formation is about the average of these two velocities. Because of the shear wave anisotropy (velocity v_{yx} is greater than the fluid velocity), the shear-pseudo-Rayleigh arrival is observed between the P and Stoneley wave arrivals.

To better understand the phenomenon, the simulation of the wave propagation is done with the borehole numerically drilled along the Z axis. A $70 \times 70 \times 300$ grid is used. All the other parameters are kept the same. The shear wave is transversely isotropic along the Z axis. The seismograms are shown in Figure 7. This time the P wave is traveling with velocity v_{zz}, which is 2740 k/m. The low frequency Stoneley waves have about the same velocity as in the Y borehole. But in the borehole along the Z axis there are no shear-pseudo-Rayleigh arrivals. This is because both v_{zx} and v_{zy} are below the fluid velocity.

Borehole Wave Propagation: Dipole

First the fluid-filled borehole is drilled along the Y axis. Other parameters are the same as the monopole simulations. The waveforms of the dipole source in the X direction are plotted in Figure 8. The seismograms are dominated by the flexural modes. Due to the strong shear wave anisotropy, there are two widely separated shear wave arrivals. The fast one is travelling with velocity v_{yx}. The slow one is travelling with velocity v_{yz}. The dipole source is aligned with the fast velocity direction (Figure 4). But the dipole source has a radiation pattern of $cos\theta$. So there is energy in the slow shear wave direction too. The slow shear wave velocity means that the small stress can produce large strain, especially when the shear wave is less than the fluid velocity. That is why the large amplitude slow shear waves show on the seismograms. On the other hand,

when the dipole source is aligned in the direction of the slow shear wave (Figure 10), there is a very small fast shear arrival shown on the seismograms. The first arrivals on the seismograms are P waves.

For the purpose of comparison the dipole waveforms are also computed in the borehole along the Z axis. The seismograms are plotted in Figure 11. In this case both shear wave velocities (v_{xz}, v_{yz}) have the same value and are less than the fluid velocity. The waveforms are dominated by the slow flexural mode.

It is very interesting to look at the wavefield snapshots. This is one of the advantages of the finite difference method. The snapshot of the X direction dipole wavefields in the borehole along the Y axis at time 1.1 ms is shown in Figure 9. This is the case of the fast and the slow shear wave splitting due to the anisotropy. It is beautifully displayed in the snapshot. The fast flexural wave is the one traveling in the first pack. The wavefields spread into the formation. The reason is that the faster shear wave velocity is greater than the borehole fluid velocity. The borehole is not a very effective waveguide. The slow flexural wave is the one trapped inside or near the borehole, because the slow shear wave velocity is less than the borehole fluid velocity. The borehole becomes a very effective waveguide for the slow flexural mode.

The snapshot of the X direction dipole wavefields in the borehole along the Z axis at time 1.1 ms is shown in Figure 12. In this case the shear wave velocity v_{zx} and v_{zy} are the same, so there is no shear wave splitting. This is exactly what the snapshot shows. The single flexural wave dominates the wavefields. The other wavefield anomaly is in the source region. The images also show vividly the good performance of the absorbing boundary condition.

In the previous examples, the dipole source and receiver are pointed in the same direction (inline dipole). Here we show one example of the dipole source and receiver that are perpendicular to each other (cross dipole). In the isotropic formation the cross dipole should be zero. But in the anisotropic formation the cross dipole log, combined with the inline dipole log, can provide very useful information about the orientation of the shear wave fast and slow directions. This information can be used to estimate the stress orientations or fluid flow directions.

For the fluid-filled borehole drilled along the Y axis, the source is pointed 45 degrees from the X axis and the receiver is 135 degrees from the X axis. The cross dipole waveforms are plotted in Figure 13. The waveforms clearly show the fast and slow shear wave arrivals. Small amplitude P waves are also shown as first arrivals. The shear wave arrivals on the cross dipole can be viewed as follows: The source dipole generates the flexural mode, which is polarized along the two principal axes (X and Z axis). Then they are superposed along the receiver direction. In this case the amplitude of the cross dipole has the same magnitude as the inline dipole. But the simulations also show that when the cross dipole direction is aligned with the principle axis its amplitude is about 100 times less than the inline dipole.

COMPARISON WITH ULTRASONIC EXPERIMENTS

Finally, the finite difference synthetics are compared with the ultrasonic lab measurements. A block of $25 \times 25 \times 15$ cm^3 phenolite solid is used to do the lab measurements. A 1.27 cm diameter hole is drilled along the X axis (Zhu et al., 1993). The experiments are carried out in a water tank. The borehole fluid is water. The transducer is built using a PZT piezoelectric tube. This tube is cut in half along the diameter and four electrodes are connected to the outer and inner sides of the two half tubes. The monopole or the dipole source can be simulated by using the same tube. When the same electric voltage is applied on the two halves of the tube, the monopole source is generated. When the opposite electric voltage is applied on the two halves of the tube, the dipole source is generated. The monopole and dipole receivers are built using the same method.

This ultrasonic model is amplified by a factor of 20 to do the finite difference simulations. The calculation grid is $320 \times 70 \times 70$. The grid size is 1 cm. The source is located at grid point (40,35,35). The receivers are located along the center of the borehole. The first receiver is 1.5 m away from the source and the receiver spacing is 0.1 m. The monopole waveforms from the finite difference simulation are plotted in Figure 14. A Kelly source with 5 kHz center frequency is used. Ultrasonic lab measurements of the monopole waveforms are plotted in Figure 15. The time scale of the lab measurements is 20 times smaller than the finite difference results. There is a 0.0072 ms time delay in the lab measurements. The receiver spacing is 0.5 cm. The finite difference results agree well with the lab measurements. Both the synthetics and the measurements very clearly show the arrivals of the P wave, the shear-pseudo-Rayleigh waves, and the low frequency large amplitude Stoneley waves. The first P wave arrival is traveling with phase velocity v_{xx}. The shear-pseudo-Rayleigh wave arrivals are caused by the fast shear wave, which is faster than the water velocity. But the Stoneley wave phase velocity is sensitive to both the fast and the slow shear waves.

The dipole waveforms from the finite difference are shown in Figure 16. The dipole source is aligned with the Y axis in the calculation. The scaled borehole model measurements are plotted in Figure 17. Both plots clearly display the fast and the slow shear wave arrivals due to the shear wave splitting in an anisotropic medium. The small P wave arrivals in the synthetics are not shown on the lab measurements because the lab measurements are low pass filtered to emphasize the two shear wave arrivals (Z. Zhu, 1993, personal communication). In general, the synthetics and the lab measurements are in good agreement.

FIELD DATA EXAMPLE

In the previous section we demonstrate that the 3-D finite difference method can provide reliable fluid-filled borehole wave propagation modeling in anisotropic formations. The goal of the 3-D finite difference borehole modeling is to interpret field logging data, especially those which cannot be explained by the simple borehole model and are difficult to process.

Data sets used here were collected by ARCO's array full waveform acoustic logging tool and shear wave logging tool. These data sets were processed before by Cheng and Cheng (1992). The shear wave velocity discrepancy between Stoneley wave inversion and the direct shear wave logging from 3720 ft to 3780 ft section is not well explained. The 3-D finite difference simulations are used here to interpret this disagreement.

The field array data from depth 3730 ft is plotted in Figure 18. The "refracted shear/pseudo-Rayleigh" is clearly shown in the last three traces between leaky P and low frequency Stoneley waves. In order to do the finite difference simulations we assume $c_{11} = c_{22} = c_{33}$, $c_{12} = c_{13} = c_{23} = c_{11} - 2c_{66}$ and $c_{44} = c_{55}$. This is similar to transverse isotropy. The formation P wave velocity and the shear wave velocities from the shear wave log and Stoneley wave inversion are used to estimate these elastic constants. They are listed in Table 4. The borehole with radius 0.12 m is drilled along the Y axis. A Kelly source of center frequency 8.5 kHz is used. A $70 \times 530 \times 70$ grid is used in the calculation.

The finite difference synthetics are shown in Figure 19. The three phases on the synthetics are matched very well with the field data. The amplitude differences are due to the fact that there are no attenuations included in the finite difference calculations. The logging tool effect is also not considered. The synthetics are clearly demonstrated "refracted shear/pseudo-Rayleigh" arrivals. One of the shear wave velocities used in the simulation is greater than the borehole fluid velocity. This confirms that the "refracted shear/pseudo-Rayleigh" arrivals are due to the fastest shear wave velocity. So the shear wave discrepancy from the shear wave log and the Stoneley wave inversion is caused by the anisotropy. The symmetry axis of the anisotropy is perpendicular to the borehole axis instead of parallel to it. The shear wave anisotropy is about 10% to 20%.

CONCLUSIONS

In this paper the 3-D finite difference method is extended into an anisotropic medium. The velocity-stress formulation is used. The scheme is second-order accuracy in time and fourth-order accuracy in space. The Higdon's absorbing boundary condition is extended into the anisotropic medium by properly chosen velocities. Once again the scheme is paralleled on the nCUBE computer.

The finite difference results agree excellently with the analytic solution of vertical force in a homogeneous transversely isotropic solid. This comparison also shows the good performance of Higdon's absorbing boundary condition in an anisotropic medium.

Borehole wave propagation in an orthorhombic phenolite formation is simulated. The nine elastic constants of the phenolite solid are determined from lab measurements. In the borehole drilled along the Z axis, the monopole log shows the P wave traveling with velocity v_{zz}. There are no shear-pseudo-Rayleigh wave arrivals due to the shear wave below the borehole fluid velocity. The dipole log is dominated by the single slow flexural mode.

In the borehole drilled along the Y axis, the monopole log shows that the P wave

is traveling with velocity v_{yy}. Because the shear wave velocity v_{yx} is greater than the borehole fluid velocity, there are shear-pseudo-Rayleigh wave arrivals shown on the monopole log between the P wave and Stoneley wave arrivals. There is shear wave splitting in the dipole log due to the anisotropy. Two shear wave arrivals correspond to the fast flexural mode and the slow flexural mode. The Stoneley wave velocity is sensitive to both the fast and the slow shear wave velocities. The cross dipole also clearly records fast and slow shear wave arrivals.

In the borehole drilled along the X axis, the monopole log shows the P wave traveling with velocity v_{xx}. The other conclusions are similar to the Y borehole. The monopole and dipole synthetics agree well with the scaled ultrasonic lab measurements.

3-D finite difference simulation is also used to explain the shear wave velocity discrepancy from field logging data.

ACKNOWLEDGMENTS

This research was supported by the Borehole Acoustics and Logging Consortium at M.I.T. and by the ERL/nCUBE Geophysical Center for Parallel Processing.

APPENDIX A:

A POINT FORCE SOLUTION IN A TRANSVERSELY ISOTROPIC SOLID

We consider the solution along the symmetry axis of a transversely isotropic solid. This analytic solution is given by Payton (1983). Define the following dimensionless parameters:

$$\begin{aligned} a &= \frac{c_{33}}{c_{44}} \\ b &= \frac{c_{11}}{c_{44}} \\ d &= \frac{1}{2}(b - \frac{c_{12}}{c_{44}}) \\ e &= 1 + ab - (\frac{c_{13}}{c_{44}} + 1)^2 \\ v_s &= \sqrt{\frac{c_{44}}{\rho}} \\ \bar{z} &= \frac{z}{v_s t} \end{aligned} \tag{A.1}$$

where $c_{11}, c_{12}, c_{13}, c_{33}$ and c_{44} are elastic constants. ρ is density. z is the distance from the source along the symmetry Z axis.

The response to the vertical force:

$$\vec{f} = (0,0,1)\delta(x)\delta(y)\delta(z)H(t) \tag{A.2}$$

where H(t) is the step function, is given by:

$$\begin{aligned} u_x &= 0 \\ u_y &= 0 \\ u_z &= \frac{1}{4\pi z v_s^2} \begin{cases} 0, & 0 < t \le t_p \\ h(\bar{z}), & t_p < t \le t_s \\ 2h(\bar{z}), & t_s < t \le t_1 \\ 1, & t > t_1 \end{cases} \end{aligned} \tag{A.3}$$

where

$$h(\bar{z}) = \frac{1}{2} - \frac{2(1-\bar{z}^2) - e + (b+1)\bar{z}^2}{2\sqrt{D}} \tag{A.4}$$

with

$$\begin{aligned} t_s &= \frac{z}{v_s} \\ t_p &= \frac{z}{\sqrt{c_{33}/\rho}} \\ t_1 &= \frac{t_s}{\bar{z}_1} \end{aligned} \tag{A.5}$$

The quantity D and $\bar{z}_1$ is given by:

$$D(\bar{z}) = [e - (b+1)\bar{z}^2]^2 - 4b(a-\bar{z}^2)(1-\bar{z}^2) \tag{A.6}$$

and

$$\bar{z}_1 = [e(b+1) - 2b(a+1) + 2\sqrt{b(1+ab-e)(a+b-e)}]^{\frac{1}{2}}/(b-1) \tag{A.7}$$

The above solution is valid for the solid satisfying the inequalities ($e < 1 + b$) and ($e^2 - 4ab < 0$). In our application the time step function is removed in the frequency domain and the source time function is convolved.

APPENDIX B

PLANE WAVE SOLUTIONS OF AN ORTHORHOMBIC SOLID

The plane wave solution of an orthorhombic solid is given by Auld (1973). In the XY plane there is a pure shear wave polarized along the Z axis,

$$v_s^2 = \frac{c_{44}cos^2\phi + c_{55}sin^2\phi}{\rho} \tag{B.1}$$

the quasi-S wave is,

$$v_{qs}^2 = \frac{c_{66} + c_{11}cos^2\phi + c_{22}sin^2\phi - \sqrt{(c_{66} + c_{11}cos^2\phi + c_{22}sin^2\phi)^2 - 4C}}{2\rho} \tag{B.2}$$

and the quasi-P wave is,

$$v_{qp}^2 = \frac{c_{66} + c_{11}cos^2\phi + c_{22}sin^2\phi + \sqrt{(c_{66} + c_{11}cos^2\phi + c_{22}sin^2\phi)^2 - 4C}}{2\rho} \tag{B.3}$$

where

$$C = (c_{11}cos^2\phi + c_{66}sin^2\phi)(c_{66}cos^2\phi + c_{22}sin^2\phi) - (c_{12} + c_{66})^2cos^2\phi sin^2\phi \tag{B.4}$$

where ϕ is the angle between propagation direction and X axis.

For propagation in the XZ plane the pure shear wave is polarized along the Y axis,

$$v_s^2 = \frac{c_{44}cos^2\theta + c_{66}sin^2\theta}{\rho} \tag{B.5}$$

the quasi-S wave is

$$v_{qs}^2 = \frac{c_{55} + c_{33}cos^2\theta + c_{11}sin^2\theta - \sqrt{(c_{55} + c_{33}cos^2\theta + c_{11}sin^2\theta)^2 - 4D}}{2\rho} \tag{B.6}$$

and the quasi-P wave is,

$$v_{qp}^2 = \frac{c_{55} + c_{33}cos^2\theta + c_{11}sin^2\theta + \sqrt{(c_{55} + c_{33}cos^2\theta + c_{11}sin^2\theta)^2 - 4D}}{2\rho} \tag{B.7}$$

where

$$D = (c_{55}cos^2\theta + c_{11}sin^2\theta)(c_{33}cos^2\theta + c_{55}sin^2\theta) - (c_{13} + c_{55})^2cos^2\theta sin^2\theta \tag{B.8}$$

In the YZ plane the pure shear wave is polarized along the X axis,

$$v_s^2 = \frac{c_{55}cos^2\theta + c_{66}sin^2\theta}{\rho} \tag{B.9}$$

the quasi-S wave is

$$v_{qs}^2 = \frac{c_{44} + c_{33}cos^2\theta + c_{22}sin^2\theta - \sqrt{(c_{44} + c_{33}cos^2\theta + c_{22}sin^2\theta)^2 - 4E}}{2\rho} \tag{B.10}$$

and the quasi-P wave is,

$$v_{qp}^2 = \frac{c_{44} + c_{33}cos^2\theta + c_{22}sin^2\theta + \sqrt{(c_{44} + c_{33}cos^2\theta + c_{22}sin^2\theta)^2 - 4E}}{2\rho} \tag{B.11}$$

where

$$E = (c_{44}cos^2\theta + c_{22}sin^2\theta)(c_{33}cos^2\theta + c_{44}sin^2\theta) - (c_{23} + c_{44})^2cos^2\theta sin^2\theta \tag{B.12}$$

where θ is the angle between propagation direction and X axis.

REFERENCES

Auld, B.A., 1973, *Acoustic Fields and Waves in Solids, Vol.1,* John Wiley & Sons, Inc.

Carcione, J.M., D. Kosloff, A. Behle, and G. Seriani, 1992, A spectral scheme for wave propagation simulation in 3-D elastic anisotropic media, *Geophysics, 57,* 1593–1607.

Chan, A.K. and L. Tsang, 1983, Propagation of acoustic waves in a fluid-filled borehole surrounded by a concentrically layered transversely isotropic formation, *J. Acoust. Soc. Am., 74,* 1605–1616.

Cheadle, S.P., R.J. Brown, and D.C. Lawton, 1991, Orthorhombic anisotropy: A physical seismic modelling study, *Geophysics, 56,* 1603–1613.

Cheng, N., and C.H. Cheng, 1992, Estimation of formation parameters using full waveform acoustic and shear wave logs, *M.I.T. Borehole Acoustic and Logging Consortium Annual Report.*

Ellefsen, K.J., 1990, Elastic wave propagation along a borehole in an anisotropic medium, *Ph.D. Thesis,* Massachusetts Institute of Technology, Cambridge, MA.

Leslie, H.D., and C.J. Randall, 1992, Multipole sources in boreholes penetrating anisotropic formations: Numerical and experimental results, *J. Acoust. Soc. Am., 91,* 12–27.

Leveille, J.P., and A.J. Seriff, 1989, Borehole wave particle motion in anisotropic formations, *J. Geophys. Res., 94,* 7183–7188.

Nicoletis, L.M., J.A. Bamberger, P.J. Quiblier, and K. Kern, 1990, Hole geometry and anisotropic effects on tube-wave propagation: a quasi-static study, *Geophysics, 55,* 167–175.

Norris, A.N., and B.K. Sinha, 1993, Weak elastic anisotrpy and the tube wave, *Geophysics, 58,* 1091–1098.

Payton, R.G., 1983, *Elastic wave propagation in transversely isotropic media,* Martinus Nijhoff Publ.

Renlie, L., and A. Raaen, 1993, Acoustic wave propgagation in a fluid-filled borehole surrounded by a formation with stress-relief-induced anisotropy, *Geophysics, 58,* 1257–1269.

Sinha, B.K., A.N. Norris, and S.K. Chang, 1991, Borehole flexural modes in anisotropic formations, *61st S.E.G. Annual Meeting Expanded Abstracts.* Houston.

Thomsen, L., 1986, Weak elastic anisotropy, *Geophysics, 51,* 1954–1966.

White, J.E., and C. Tongtaow, 1981, Cylindrical waves in transversely isotropic media, *J. Acoust. Soc. Am., 70,* 1147–1155.

Zhu, Z., C.H. Cheng, and M.N. Toksöz, 1993, Propagation of flexural waves in an azimuthally anisotropic borehole model, submitted to *Geophysics*

Quantity	Value
c_{11}	66.6 GPa
c_{12}	19.7 GPa
c_{13}	39.4 GPa
c_{33}	39.9 GPa
c_{44}	10.9 GPa
ρ	2590 kg/m^3

Table 1: Properties of the transversely isotropic medium, which represents Mesaverde clay shale.

Direction	P wave velocity (m/s)
45 degrees to Y,Z axes 90 degrees to X axis	3200
45 degrees to X,Z axes 90 degrees to Y axis	3300
45 degrees to X,Y axes 90 degrees to Z axis	3900

Table 2: The P wave velocities measured between opposite edges of the phenolite cube (Z. Zhu, 1993, personal communication).

Quantity	Value
c_{11}	20.80 GPa
c_{12}	11.47 GPa
c_{13}	7.26 GPa
c_{22}	17.46 GPa
c_{23}	7.87 GPa
c_{33}	10.06 GPa
c_{44}	2.59 GPa
c_{55}	2.59 GPa
c_{66}	5.04 GPa
ρ	1340 kg/m^3

Table 3: Properties of the orthorhombic medium, which represents Phenolic XX-324.

Quantity	Value
c_{11}	22.7 GPa
c_{12}	11.7 GPa
c_{13}	11.7 GPa
c_{22}	22.7 GPa
c_{23}	11.7 GPa
c_{33}	22.7 GPa
c_{44}	3.36 GPa
c_{55}	3.36 GPa
c_{66}	5.5 GPa
ρ	2150 kg/m^3

Table 4: Elastic properties used in the simulation of field logging data

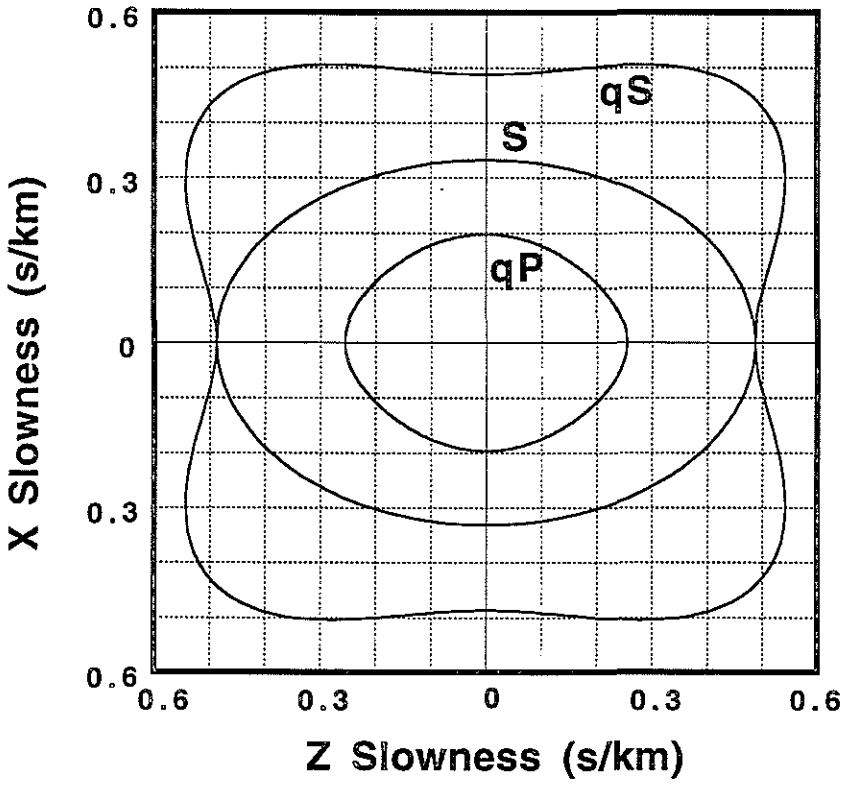

Figure 1: Slowness surfaces of Mesaverde clay shale. There are three modes, pure shear, quasi-P, and quasi-S.

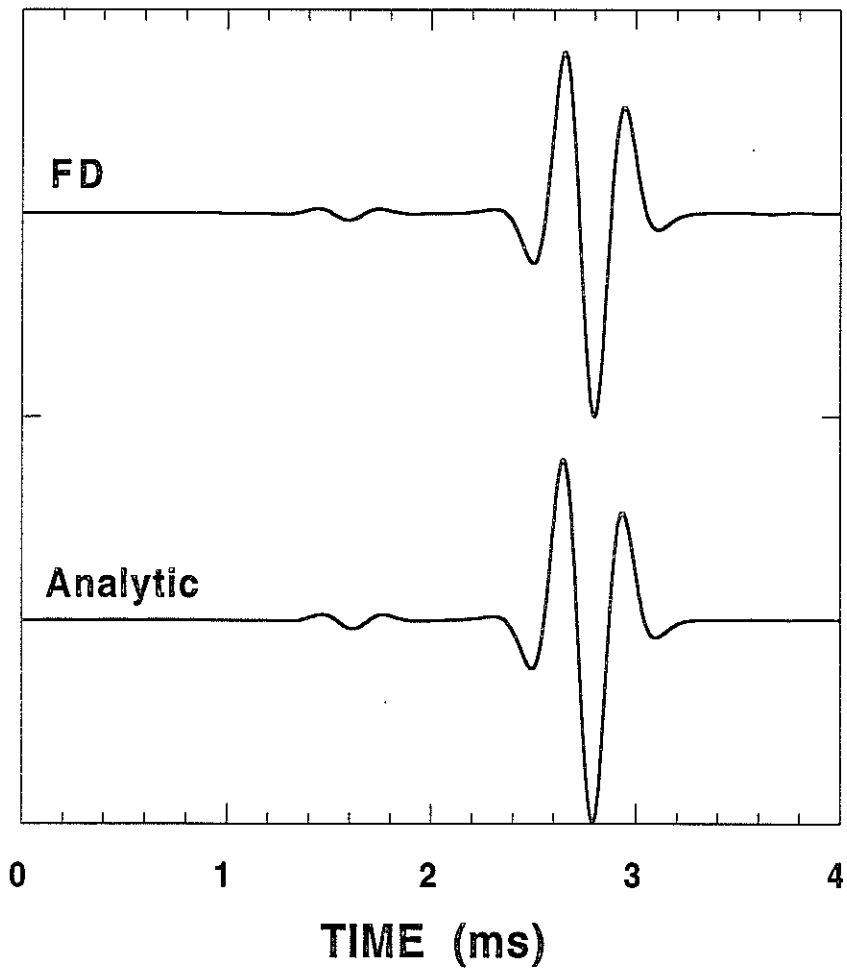

Figure 2: Comparison of finite difference result (FD) with analytic solution of a vertical point force in homogeneous transversely isotropic medium. The source center frequency is 2.5 kHz. Both amplitudes are normalized

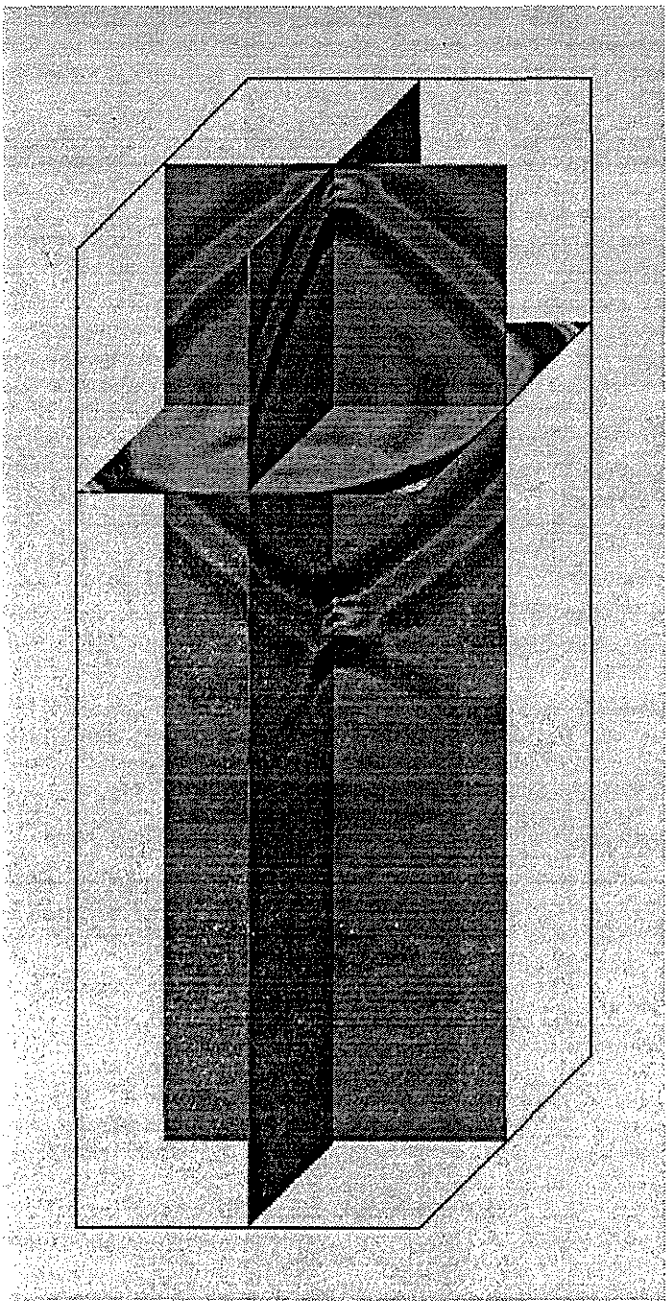

Figure 3: The snapshot of the velocity v_z wavefield from a vertical point force in a homogeneous transversely isotropic medium at time 1.6 ms. Source center frequency is 2.5 kHz. The image size is $70 \times 70 \times 200$.

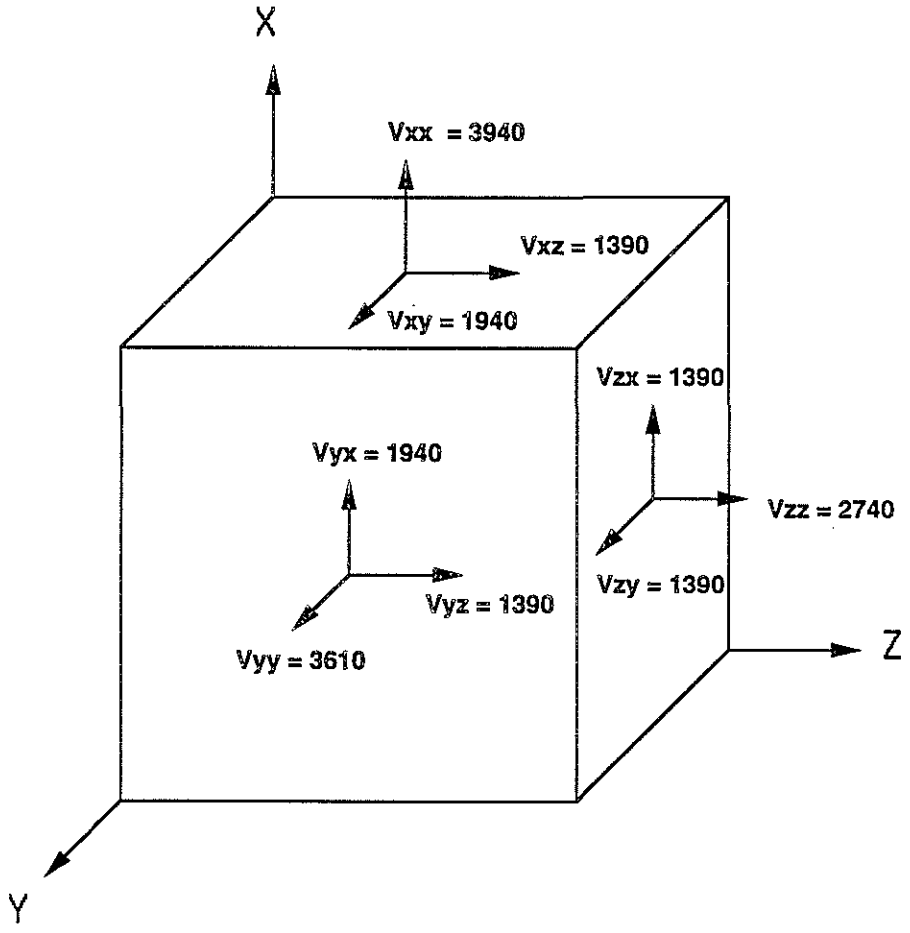

Figure 4: The P and S wave velocities measured along the three principal axes of a phenolite cube. The velocity is given with two indexes. The first index is the propagation direction and the second index is the particle motion direction (after Zhu et al., 1993).

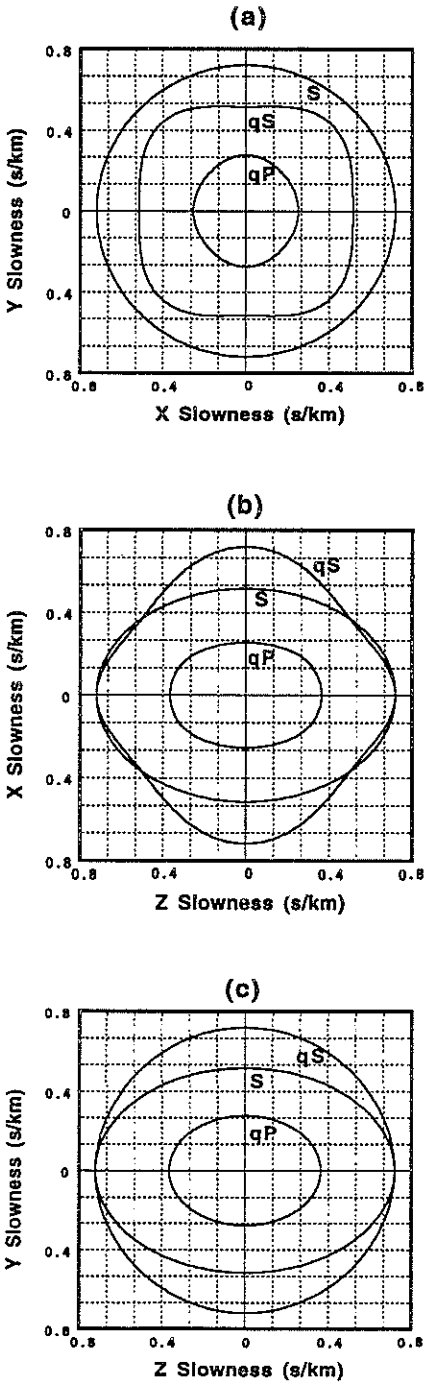

Figure 5: Slowness surfaces of phenolite solid. There are three modes, pure shear, quasi-P, and quasi-S. (a) X-Y plane. (b) X-Z plane. (c) Y-Z plane

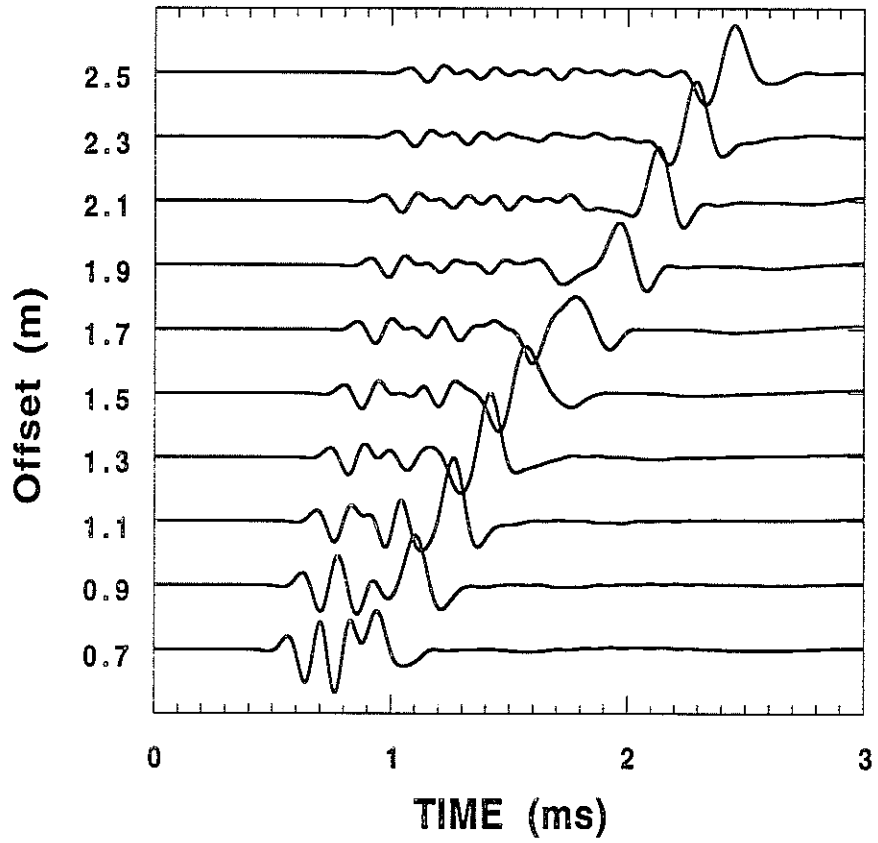

Figure 6: Monopole seismograms of fluid-filled borehole drilled along the Y axis in phenolite formation. Source center frequency is 5 kHz.

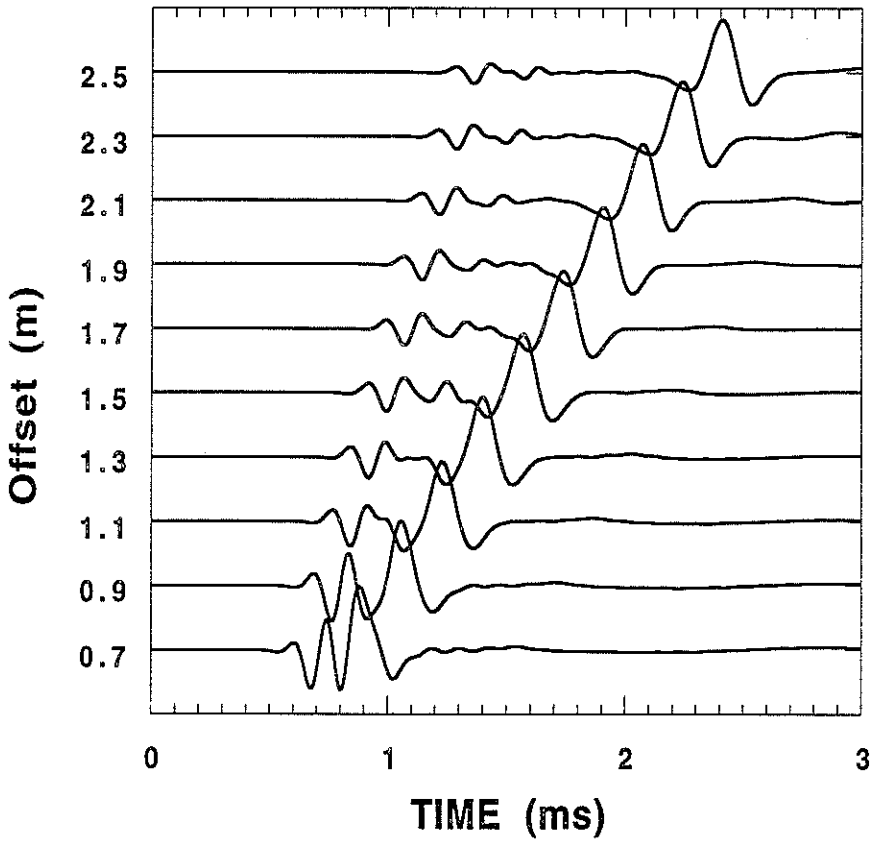

Figure 7: Monopole seismograms of a fluid-filled borehole drilled along the Z axis in a phenolite formation. Source center frequency is 5 kHz.

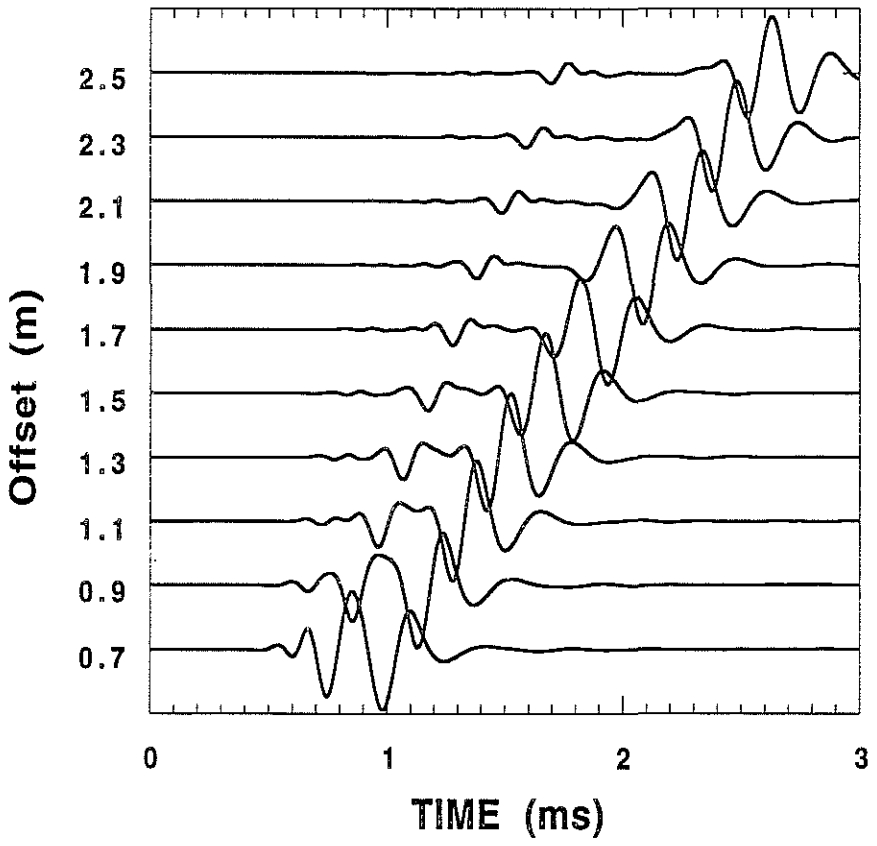

Figure 8: Dipole seismograms from a fluid-filled borehole drilled along the Y axis in a phenolite formation. Source center frequency is 5 kHz and dipole is in the X direction.

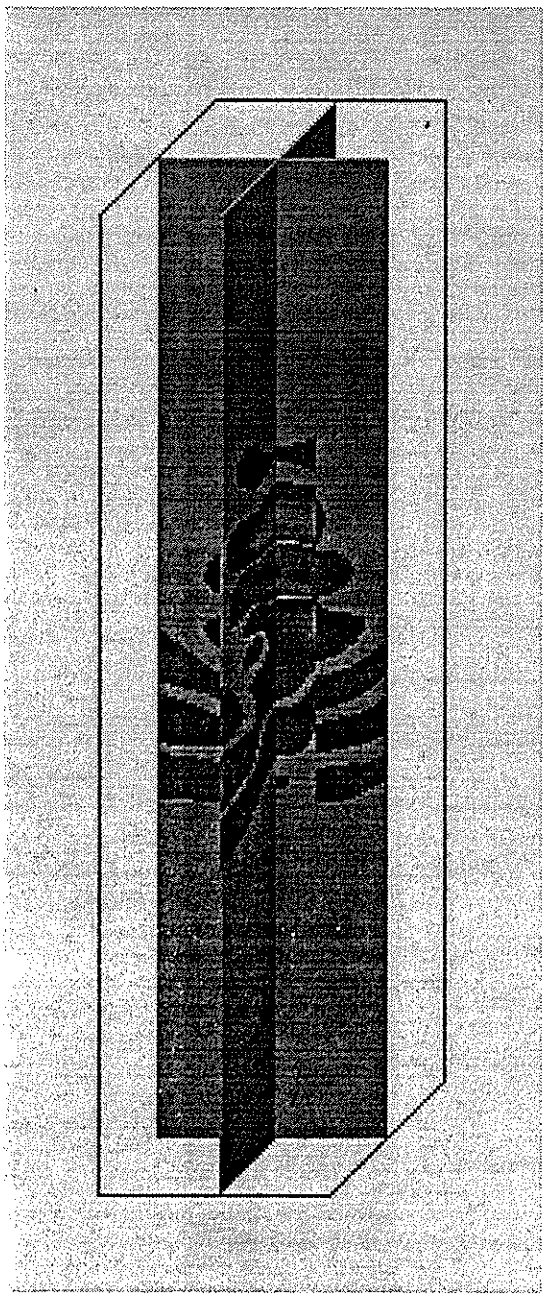

Figure 9: Wavefield image from a dipole source at time 1.1 ms. The fluid filled borehole is drilled along the Y axis in a phenolite formation. The vertical direction is the Y axis. Source center frequency is 5 kHz and the dipole is in the X direction.

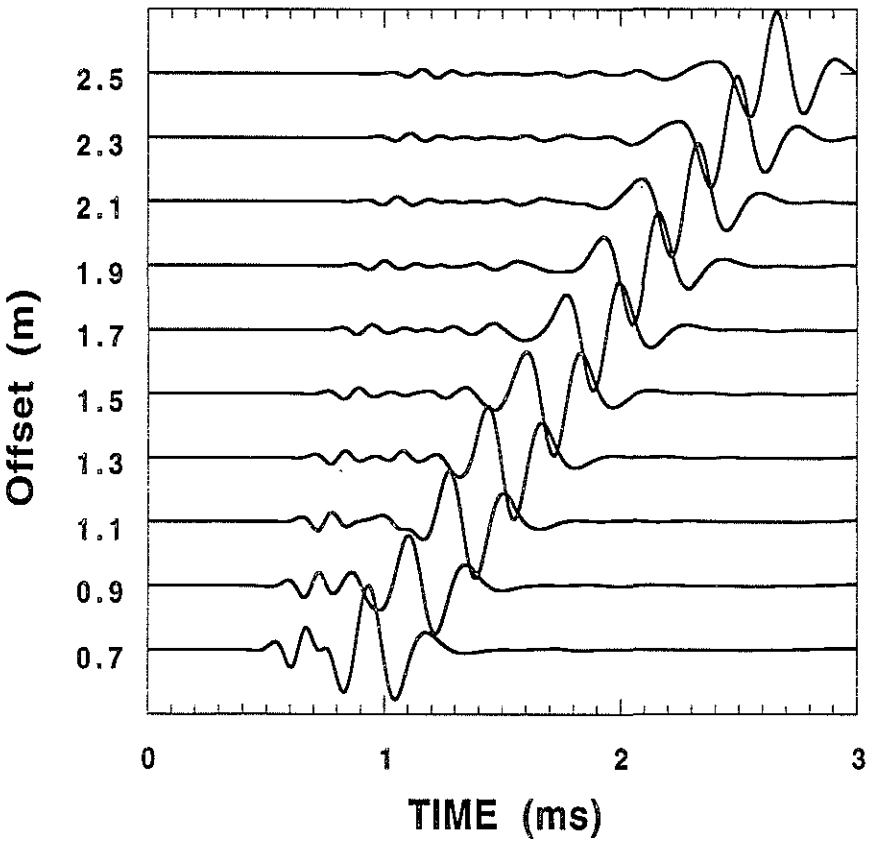

Figure 10: Dipole seismograms from a fluid-filled borehole drilled along the Y axis in a phenolite formation. Source center frequency is 5 kHz and the dipole is in the Z direction.

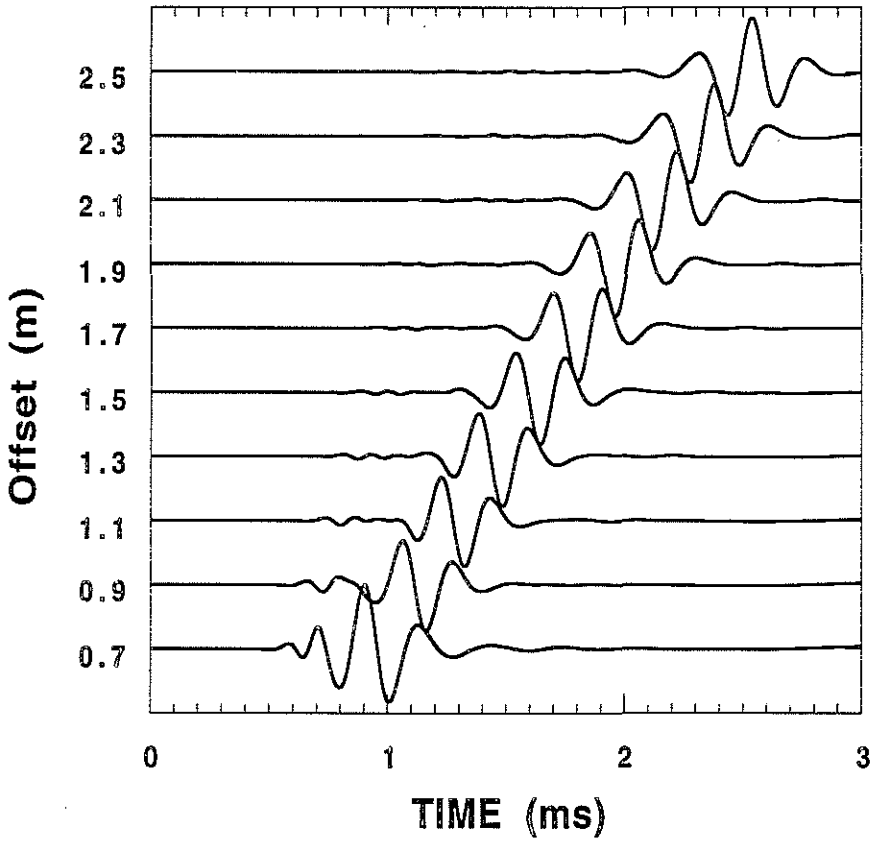

Figure 11: Dipole seismograms from a fluid-filled borehole drilled along the Z axis in a phenolite formation. Source center frequency is 5 kHz and the dipole is in the X direction.

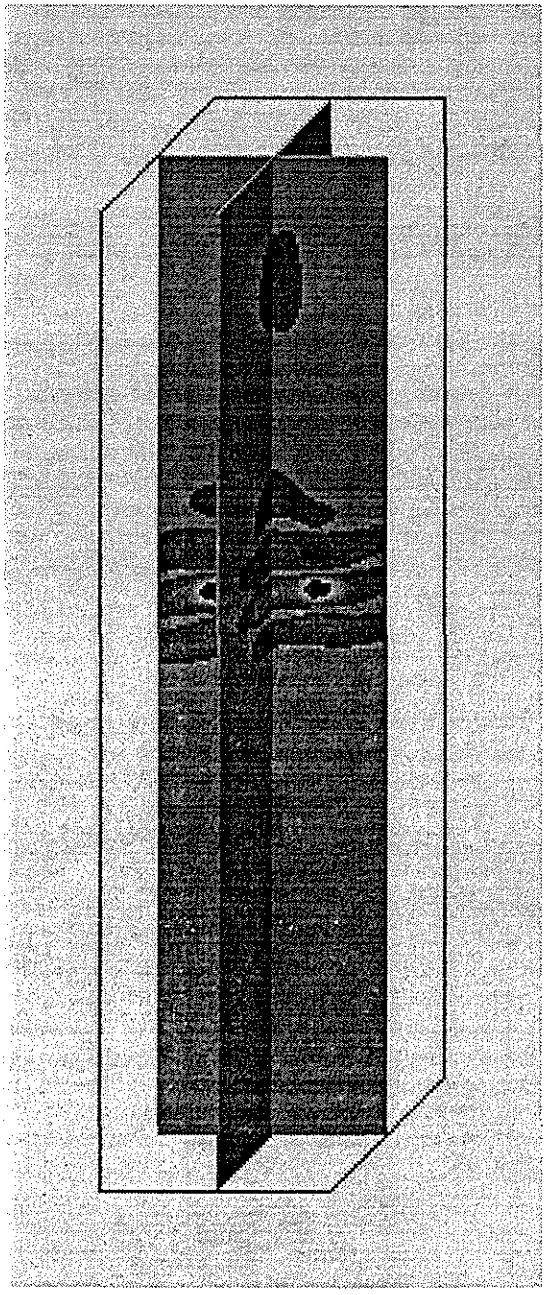

Figure 12: Wavefield image from a dipole source at time 1.1 ms. The fluid filled borehole is drilled along the Z axis. Source center frequency is 5 kHz and the dipole is in the X direction.

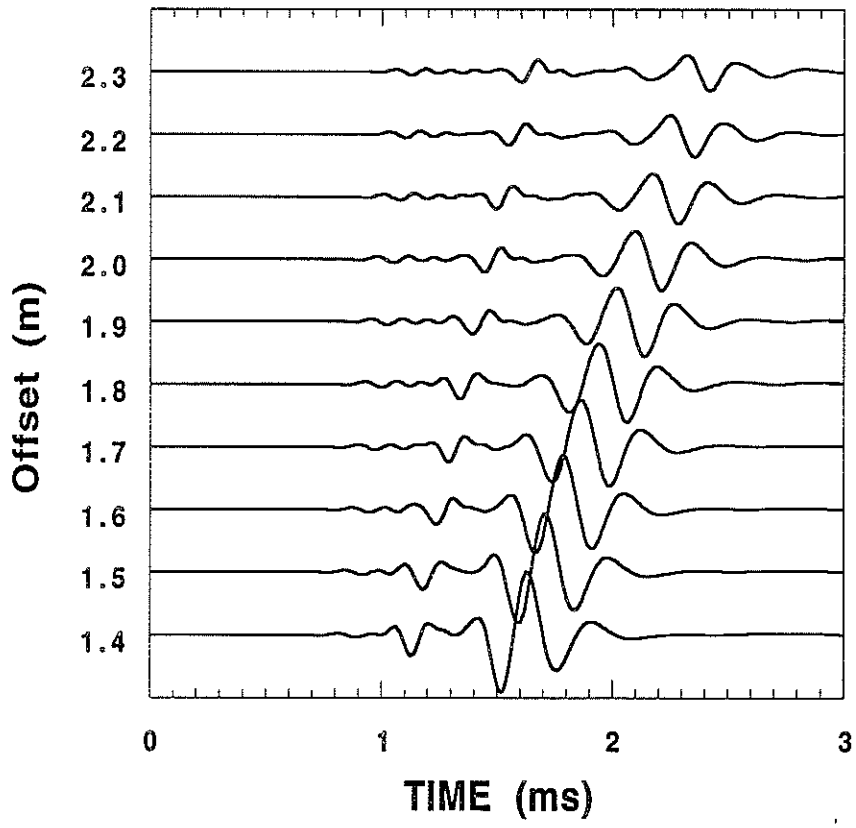

Figure 13: Cross dipole seismograms from a fluid-filled borehole drilled along the Y axis in a phenolite formation. Source center frequency is 5 kHz. The source dipole is 45 degrees from the X axis and the receiver dipole is 135 degrees from the X axis.

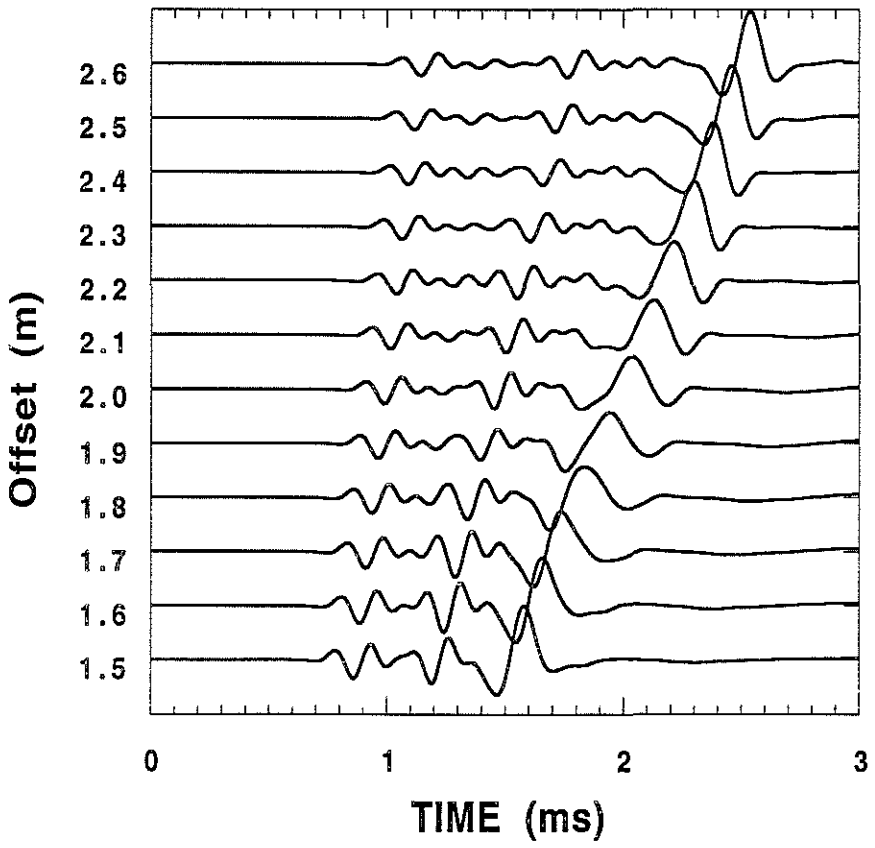

Figure 14: Finite difference monopole seismograms from the fluid-filled borehole drilled along the X axis in a phenolite formation. Source center frequency is 5 kHz.

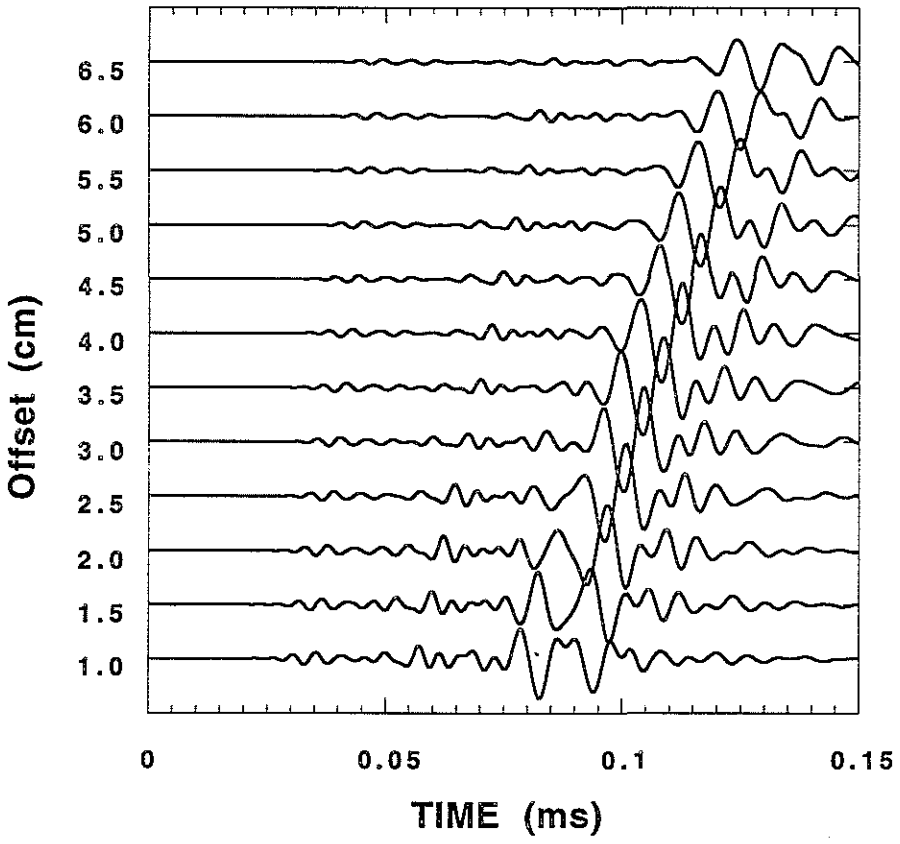

Figure 15: Ultrasonic lab measurement of monopole seismograms from the fluid-filled borehole drilled along the X axis in a phenolite solid. (After Zhu et al., 1993)

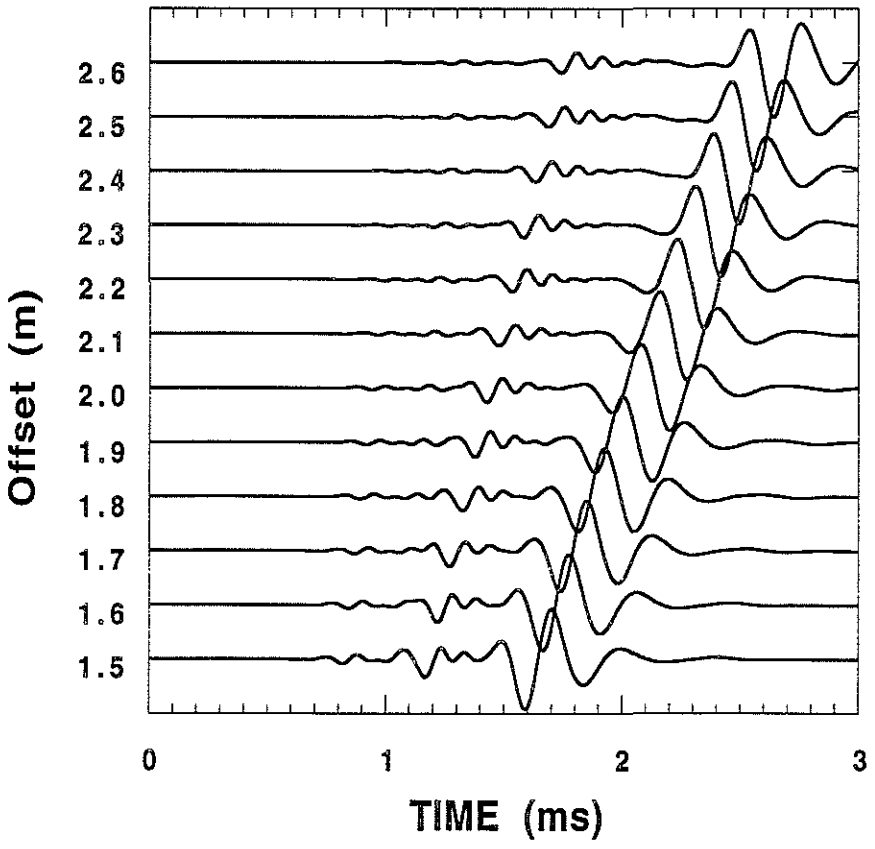

Figure 16: Finite difference dipole seismograms from the fluid-filled borehole drilled along the X axis in a phenolite formation. Source center frequency is 5 kHz.

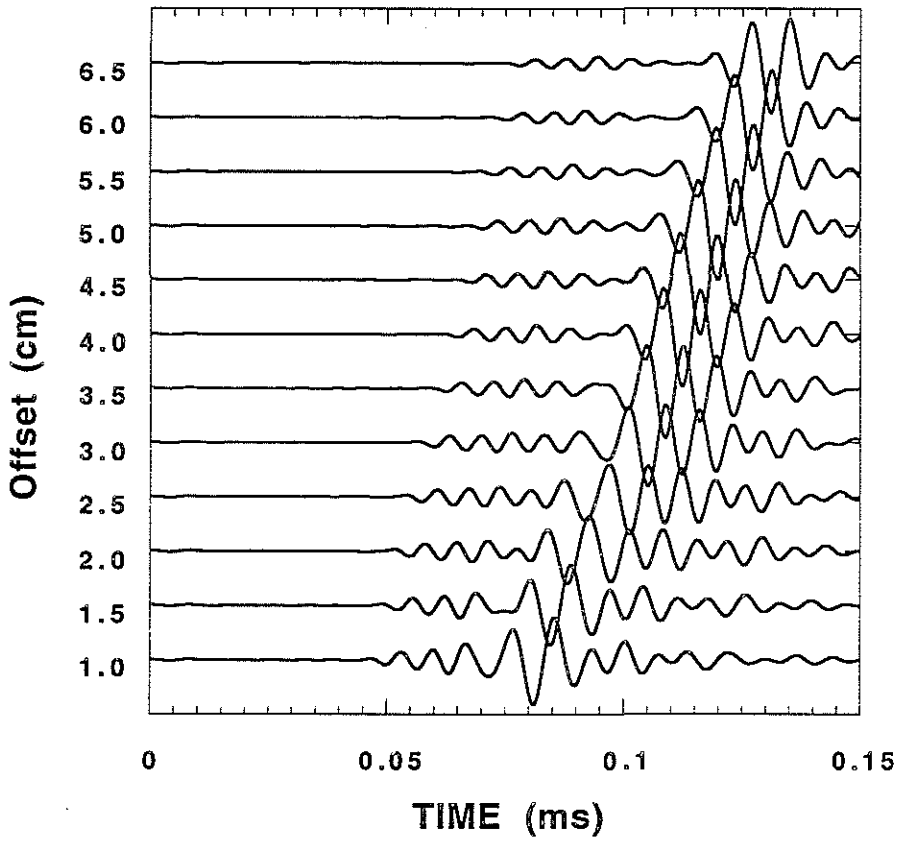

Figure 17: Ultrasonic lab measurement of dipole seismograms of a fluid-filled borehole drilled along the X axis in a phenolite solid. (After Zhu et al., 1993)

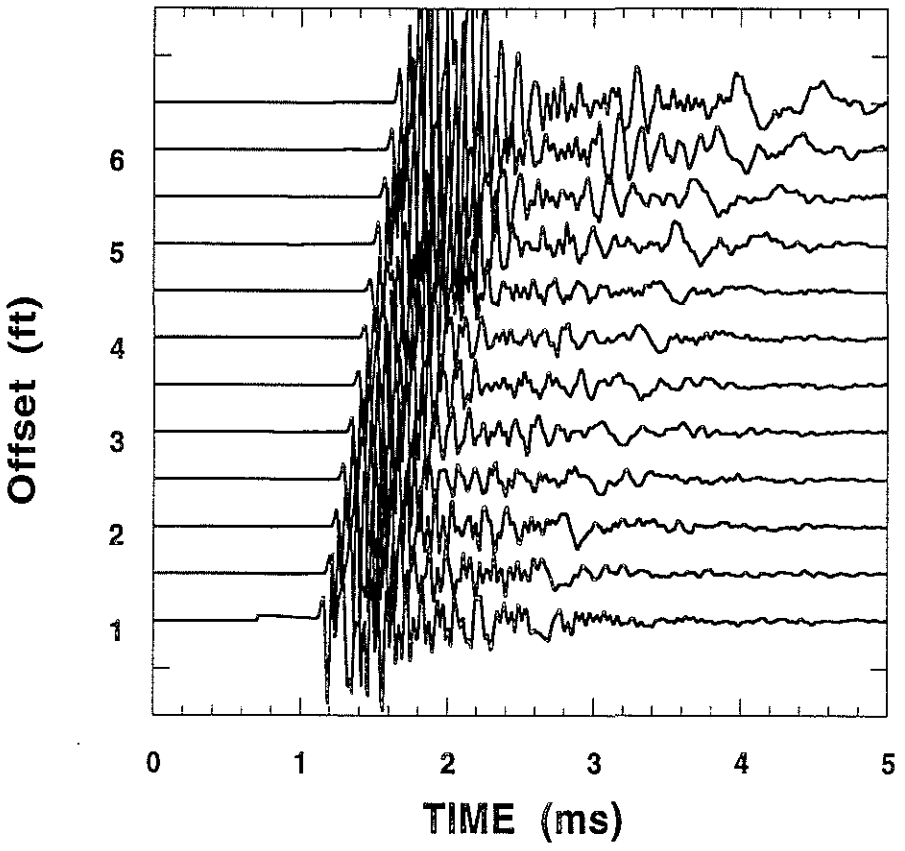

Figure 18: Field array sonic tool data from depth 3730 ft. There are 12 traces.

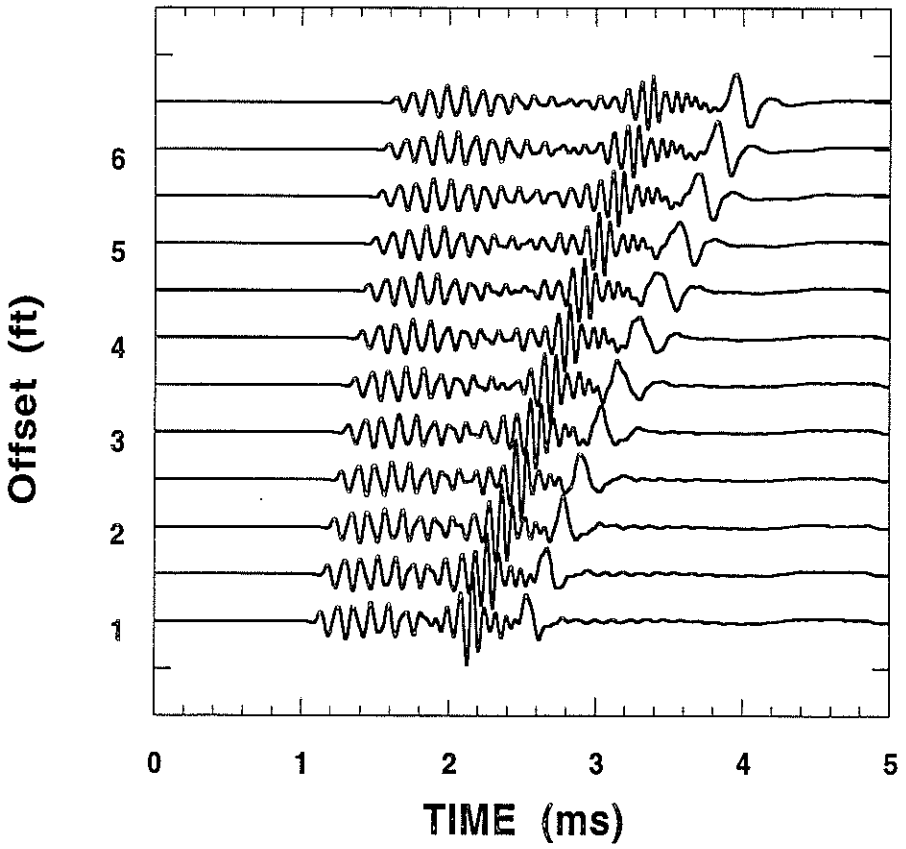

Figure 19: 3-D finite difference synthetics for array sonic logging at depth 3730 ft. The source center frequency is 8.5 kHz.